Satellite multiangle cumulus geometry retrieval: Case study

Evgueni Kassianov, Thomas Ackerman, Roger Marchand, and Mikhail Ovtchinnikov

Pacific Northwest National Laboratory, Richland, Washington, USA

[1]   Most satellite-based analyses have been conducted using near-nadir viewing sensors. The Multiangle Imaging Spectroradiometer (MISR), recently launched on the NASA Terra platform, provides high-resolution measurements of reflectance at nine different viewing angles. In this study, we examine the possible retrieval of detailed cumulus geometry using the new and unique MISR data sets. We suggest one approach and apply it to an early MISR data set of small marine cumulus clouds. This paper also presents validation analysis of this technique with both independent, ground-based radar measurements and a model-output inverse problem. Collocated and coincident MISR data and ground-based observations at the Atmospheric Radiation Measurement Tropical Western Pacific site form the basis of this validation. Future work will attempt to test the suggested approach with additional MISR scenes.   *INDEX TERMS:* 3359 Meteorology and Atmospheric Dynamics: Radiative processes; 3360 Meteorology and Atmospheric Dynamics: Remote sensing; 3374 Meteorology and Atmospheric Dynamics: Tropical meteorology; 3394 Meteorology and Atmospheric Dynamics: Instruments and techniques; *KEYWORDS:* inhomogeneous clouds, multidirectional observations, satellite measurements, cloud radar

1.   Introduction

[2]   Satellite remote sensing is the major source for gathering statistics of cloud properties; however, accurate and robust methods for extracting both optical and geometrical characteristics of broken clouds have yet to be fully developed. Currently, most cloud retrieval schemes rely on spectral (e.g., microwave, visible, or IR) observations from near vertically pointing remote sensors [*Minnis et al.*, 1992; *Rossow*, 1989; *Rossow and Schiffer*, 1999; *Chevallier et al.*, 2001]. Although the multispectral techniques can provide reasonable retrievals of cloud fraction and mean optical depth, the estimation of other important geometrical parameters, such as cloud vertical thickness, is not as reliable. The cloud morphology and cloud height are important for both radiative budget climate investigations and cloud type classifications [e.g., *Wang and Sassen*, 2001] and can be obtained from multiangle satellite observations [see *Diner et al.*, 1999, and references therein].

[3]   In this paper, we demonstrate how the horizontal distribution of cloud pixels and their vertical geometrical thickness can be reconstructed from multiangle satellite observations. Physically, the suggested approach is based on two dependences: (1) For a fixed horizontal cloud distribution the probability of a clear line of sight is a monotonically decreasing function of zenith viewing angle, and (2) the rate of decrease of this probability depends on the vertical cloud size stratification. We assume that these

dependences are valid for the majority of single-layer broken clouds. The study is focused on the special case of small marine cumulus clouds observed by the Multiangle Imaging Spectroradiometer (MISR), recently launched on the NASA Terra Platform. To validate the suggested approach, we used collocated and coincident MISR data and independent ground-based radar observations at the Atmospheric Radiation Measurement (ARM) Tropical Western Pacific (TWP) site at Nauru Island. In addition, we tested this approach with a model-output inverse problem.

[4]   In section 2 of this paper the suggested approach is introduced. Application of this approach to the real MISR-data cloud retrieval is discussed in section 3. Also, section 3 includes validation analysis with ground-based radar measurements. In section 4 the model-output inverse problem is presented. Section 5 summarizes the results.

2.   Approach

[5]   There are two basic steps to the suggested approach. The first step (section 2.2) is the detection of cloud pixels. To separate cloud pixels from noncloud pixels, we used a new cloud analysis that relies on angular signatures of measured radiances. The output of this analysis is the horizontal distribution of cloud pixels (clouds). The second step (section 2.3) is to obtain the vertical geometrical size of cloud pixels. Two simple models, which convert the nadir radiance to the cloud vertical geometrical thickness, were applied. The values of cloud geometrical thickness were forced to agree with multiangular MISR observa-

tions. These two steps are based on the directional cloud fraction.

2.1. Directional and Average Cloud Fraction

[6] Among fundamental parameters describing the geometry of broken clouds is the directional cloud fraction $N(\theta) = 1 - P_{clear}(\theta)$, where $P_{clear}(\theta)$ is the probability of a clear line of sight at zenith viewing angle (θ). The directional cloud fraction $N(\theta)$ depends on the nadir-view cloud fraction N_{nadir}, the horizontal cloud distribution (e.g., random, clustered, or regular), and vertical cloud size variability. In the general case an empirical expression for $N(\theta)$ can be formulated on the basis of field data or results of model simulations. For some cloud models an analytical expression can be obtained in terms of cloud bulk geometrical parameters [*Titov*, 1990; *Han and Ellingson*, 1999]. As an example, for a broken cloud field composed of randomly placed parallelepipeds with identical and constant geometrical thickness h, the directional cloud fraction is given by [*Titov*, 1990]

$$N(\theta) = 1 - P_{clear}(\theta) = 1 - (1 - N_{nadir}) \exp\left(\frac{\rho h \tan(\theta)}{D}\right), \quad (1)$$

where ρ and D are the model parameter and the average horizontal cloud size, respectively.

[7] The geometrical thickness h of broken clouds can vary strongly in space, so that the directional cloud fraction $N(\theta)$ may be dependent not only on the first moment (the average vertical cloud size H) but also on higher statistical moments describing the h variations. The following simple example (Figure 1) shows qualitatively how variations of cloud top height influence the directional cloud fraction $N(\theta)$. We consider a two-dimensional (2-D) cloud (a cloud infinite in the y direction), assuming that the cloud consists of just three pixels with the same horizontal size L (cloud horizon-
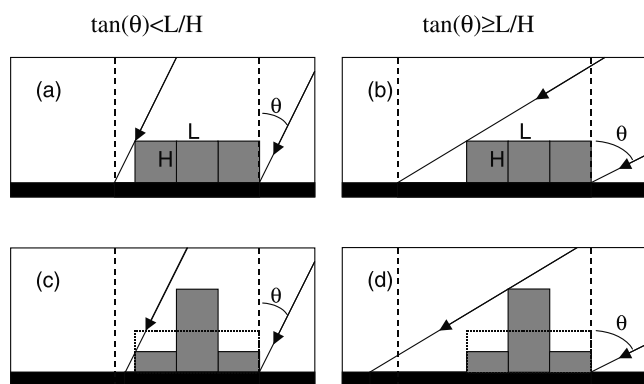
Figure 1. A schematic diagram illustrating that the directional cloud fraction (cloud projection onto x axis) depends on the cloud geometrical thickness distribution in addition to the average vertical cloud size H (see text for details). (a and c) Small viewing angles. For variable cloud top the directional cloud fraction $N(\theta)$ can be smaller (Figure 1c) than $N(\theta)$ for constant cloud top (Figure 1a). (b and d) Large viewing angles. For variable cloud top $N(\theta)$ can be larger (Figure 1d) than $N(\theta)$ for constant cloud top (Figure 1b).

Table 1. Nine Multiangle Imaging Spectroradiometer Cameras With Corresponding Look Angles

Direction	Camera	Look Angle, θ
Forward	Df	70.5
	Cf	60.0
	Bf	45.6
	Af	26.1
Nadir	An	0.0
Aft	Aa	26.1
	Ba	45.6
	Ca	60.0
	Da	70.5

tal size is $D = 3L$) and the same cloud base Hb ($Hb = 0$). Let us consider two cases. For case 1 all pixels have the same vertical size H. For case 2 the first and third pixels have the same vertical size $h_{min} = H/2$, while the vertical size of the second (middle) pixel is $h_{max} = 2H$. Obviously, both cases 1 and 2 have identical mean vertical size H. From simple geometrical considerations it follows that, for slant viewing directions, the directional cloud fraction $N(\theta)$ (cloud projection onto the x axis) will be $D + H \tan(\theta)$ for case 1, while for case 2 the size of the geometrical shadow will be $D + \tan(\theta)h_{min}$ if $(h_{max} - h_{min})\tan(\theta) \leq L$ and $D - L + \tan(\theta)h_{max}$ if $(h_{max} - h_{min})\tan(\theta) > L$. Thus for the same horizontal D and mean vertical H cloud sizes the directional cloud fraction $N(\theta)$, corresponding to the case with irregular cloud top boundary (case 2), can either be greater (Figures 1b and 1d) or less (Figures 1a and 1c) than the directional cloud fraction $N(\theta)$, corresponding to the case with plane-parallel cloud geometry (case 1). For a cloud field the dependence of $N(\theta)$ on cloud shape will be even more complex because of the effects of mutual cloud shadowing. These effects, in turn, depend on the horizontal cloud distribution and vertical cloud structure.

[8] High-resolution ($\Delta x \sim 0.275$ km) observations at nine viewing angles and four wavelengths (446, 558, 672, and 866 nm) are available from the MISR, recently launched on the NASA Terra platform. The observational characteristics of the MISR instrument are provided at the MISR Web page (http://eos-am.gsfc.nasa.gov/misr.html). These nine viewing angles $\theta = \{\theta_i, i = 1, \ldots, 9\}$ spread out along the flight path in the forward and aft directions (Table 1). Note that multiangle MISR observations are nearly simultaneous: Time interval between measurements of Df and Da cameras is $\sim$7 min [*Diner et al.*, 1999]. We assume that cloud fields do not change significantly (in statistical sense) during this time interval. Since the MISR instrument measures reflectance in nine viewing directions, it seems reasonable to use all this information for h retrieval. To do that, we introduce an average cloud fraction N_{avr} defined as

$$N_{avr} = \frac{1}{n}\sum_{i=1}^{n} N(\theta_i), \quad n = 9, \quad (2)$$

where $N(\theta_5) = N_{nadir}$. Below we discuss how the directional cloud fraction $N(\theta)$ can be retrieved from satellite data.

2.2. Average Cloud Fraction and Radiance Threshold

[9] Given a set of measured radiances at a single angle $I(\theta)$, a corresponding probability density function pdf$\{I(\theta)\}$

can readily be obtained that satisfies the normalization condition

$$\int_{I_{\min}(\theta)}^{I_{\max}(\theta)} \mathrm{pdf}\{I(\theta)\}\, dI(\theta) = 1, \qquad (3)$$

where $I_{\min}(\theta)$ and $I_{\max}(\theta)$ are the minimum and maximum radiances, respectively. One can define the directional cloud fraction $N_{\mathrm{misr}}(\theta)$ as

$$N_{\mathrm{misr}}(\theta) = \int_{I_0(\theta)}^{I_{\max}(\theta)} \mathrm{pdf}\{I(\theta)\}\, dI(\theta), \qquad (4)$$

where $I_0(\theta)$ is a radiative threshold. It follows from equation (4) that $N_{\mathrm{misr}}(\theta)$ is simply the fraction of the measured radiance $I(\theta)$, which exceeds radiative threshold $I_0(\theta)$.

[10] Here and below the subscript "misr" on $N(\theta)$ and other variables indicates that they are obtained on the basis of equation (4). We emphasize that the threshold $I_0(\theta)$ depends on cloud geometrical and optical properties, atmospheric and surface parameters, and illumination conditions (solar zenith and azimuth angles). Presently, no reliable methods are available to select a threshold set $\mathbf{I}_0(\theta) = \{I_0(\theta_i)\ i = 1,\dots, 9\}$ unambiguously; hence the use of $N_{\mathrm{avr,misr}}$ for an h retrieval is not generally justified. Now we consider an alternative parameter:

$$\Delta N = N_{\mathrm{avr}} - N_{\mathrm{nadir}}. \qquad (5)$$

[11] For a fixed horizontal distribution of cloud pixels the parameter ΔN characterizes the relative influence of the vertical geometrical thickness h of cloud pixels on N_{avr}. For example, if the cloud aspect ratio $H/D \ll 1$, then $N(\theta) \sim N_{\mathrm{nadir}}$, and $N_{\mathrm{avr}} \sim N_{\mathrm{nadir}}$. If the cloud aspect ratio $H/D \geq 1$, then $N(\theta) > N_{\mathrm{nadir}}$, and $N_{\mathrm{avr}} > N_{\mathrm{nadir}}$. According to equations (2) and (4), ΔN_{misr} is a function of nine parameters $I_0(\theta_i)$, $i = 1, \dots, 9$. Therefore a change to a single relative variable can be useful. Here this was done in the following way: To perform a calculation of $N_{\mathrm{misr}}(\theta_i)$, $i = 1,\dots, 9$, steps (bins) $\Delta I(\theta_i) = [I_{\max}(\theta_i) - I_{\min}(\theta_i)]/M$ were selected. The parameter M, which will be referred to as the number of radiance bins, was set to be equal for all θ_i, $i = 1, \dots, 9$. In this case, $I_0(\theta_i) = I_{\min}(\theta_i) + m \times \Delta I(\theta_i)$, $i = 1, \dots, 9$, and ΔN_{misr} depend on just one relative variable (digital count) m: $m = 1, \dots M$.

[12] Recall that the h retrieval algorithm proposed here consists of the following two basic steps: (1) detecting cloud pixels and (2) obtaining their vertical geometrical sizes. First, a relative value $m = m^*$ is determined, at which $\Delta N_{\mathrm{misr}}(m^*)$ peaks. This maximum value $\Delta N_{\mathrm{misr}}(m^*)$ allows one to specify radiative threshold uniquely. We test the validity of this specification later (sections 3.3–3.6 and section 4). Second, an absolute threshold is selected for nadir radiance: $I_0^*(\theta_5) = I_{\min}(\theta_5) + \Delta I(\theta_5) \times m^*$. This value $I_0^*(\theta_5)$ is then used for determining horizontal cloud distribution. Specifically, the condition $I(\theta_5) > I_0^*(\theta_5)$ is checked for each pixel. All pixels satisfying this condition are flagged as 100% cloud coverage; all other pixels are background (clear-sky). Finally, for the fixed horizontal distribution of clouds the parameters of the chosen cloud model discussed in section 2.3 are adjusted such that $\Delta N_{\mathrm{mod}} = \Delta N_{\mathrm{obs}}(m^*)$.

[13] Note that the cloud properties (e.g., the nadir-view cloud fraction), derived by using the suggested retrieval algorithm, and the physical cloud properties are not necessarily the same. The selection of radiance (reflectance) threshold is always a potential contributor of difference between cloud properties obtained with a radiative threshold and a physical cloud property threshold [see, e.g., *Rossow*, 1989]. We validate the suggested method with both independent ground-based radar measurements (sections 3.3– 3.6) and a model-output inverse problem (section 4).

2.3. Cloud Model Specification

[14] To determine ΔN_{mod}, we need to select a cloud model. In other words, we have to establish a rule by which to determine the geometrical thickness of each cloud pixel. Recently, a few models that relate the geometrical thickness h to the optical thickness τ of the cloudy pixels have been suggested [*Minnis et al.*, 1992; *Chambers et al.*, 2001]. The optical thickness can be determined by the independent pixel approximation (IPA), whose accuracy degrades with increasing horizontal inhomogeneity of the broken cloud field and/or increasing horizontal resolution of cloud observations [see, e.g., *Barker and Liu*, 1995; *Chambers et al.*, 1997; *Varnai and Marshak*, 2001]. The cumulus clouds are highly inhomogeneous (Figure 3); therefore the use of the IPA for an accurate h retrieval with high spatial resolution ($\Delta x \sim 0.275$ km) would be rather problematic. Moreover, additional assumptions about the effective particle radius and the total droplet concentration should be used to convert the cloud optical thickness τ to the cloud vertical size h [*Pawlowska et al.*, 2000; *Chambers et al.*, 2001].

[15] The cloud model used here was chosen on the basis of the following general considerations. First, geometrically thick pixels typically have a large nadir radiance (or reflectance), but for geometrically thin pixels the reverse is true. Second, the nadir radiance depends nonlinearly on the geometrical thickness. The analysis of the model radiative transfer simulations in 3-D broken clouds showed that the relationship between the geometrical cloud thickness h and the nadir reflectance R can be approximated with the simple formula $h = a + b\sqrt{R}$ (the optical depth τ of cloud pixels is varied through a large range $5 \leq \tau \leq 50$). As an illustration, let us consider the model results (Figure 2) obtained for a 3-D cloud field that was derived from radiances measured by the Landsat 5 Thematic Mapper instrument. This 3-D cloud field was used in the International Intercomparison of 3D Radiation Codes (I3RC) (see Web page at http://climate.gsfc.nasa.gov/I3RC). From Figure 2, one can see that the linear regression can be applied to specify the functional relationship between h and $\sqrt{R}$; the correlation coefficient is ~ 0.95 for both values of solar zenith angle. We evaluate the sensitivity of the h retrieval to the choice of different cloud models. At our initial exploratory stage it is reasonable to use a simple expression to approximate this nonlinear dependence. We chose to use the following two simple models: Model 1 assumes that for each cloud pixel the vertical cloud height was taken to be linear dependence on the square root of the nadir radiance $I(\theta_5)$:

$$h_{\mathrm{mod},1} = a_1 + b_1 \sqrt{I(\theta_5)}. \qquad (6a)$$
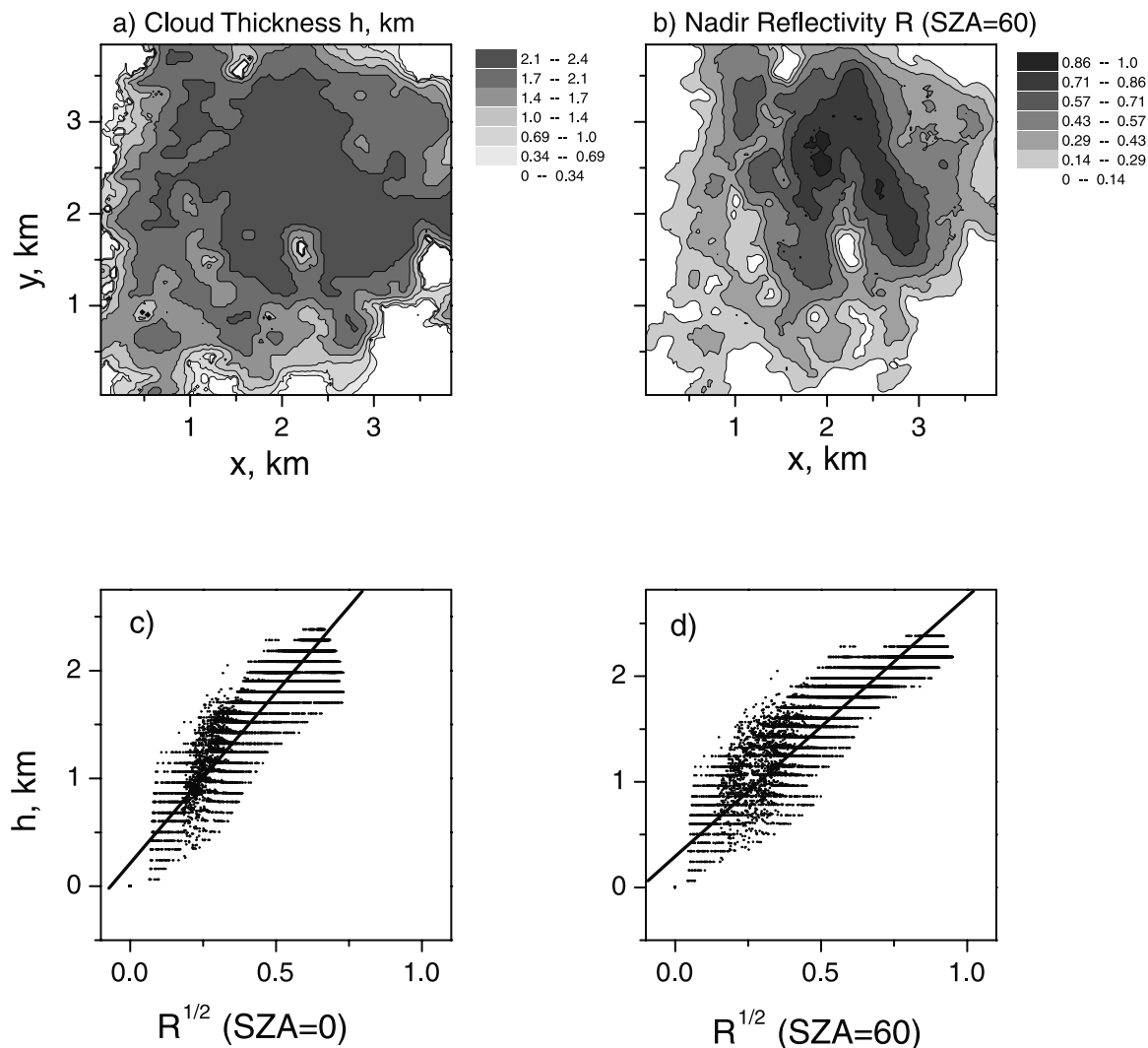
Figure 2. (a) Landsat-derived cloud thickness h, (b) simulated nadir reflectivity R (solar zenith angle (SZA) = 60) for the Landsat-derived cloud field and scatterplots of the cloud thickness h versus the square root of the nadir reflectivity $R^{1/2}$ for (c) SZA = 0 and (d) SZA = 60.

Model 2 assumes that for each cloud pixel, the vertical cloud height was taken to be linear dependence on the natural logarithm of the nadir radiance $I(\theta_5)$:

$$h_{\mathrm{mod},2} = a_2 + b_2 \ln\{I(\theta_5)\}. \qquad (6b)$$

[16] The coefficients in both models are obtained by fitting the model to the observations. A set of coefficients is found for each assumed average geometrical thickness. In section 3.4 we estimate the sensitivity of the suggested technique to the model specification.

3. MISR Data Cloud Retrieval

3.1. Satellite and Ground-Based Data

[17] To validate the multiangle retrieval technique, we use available satellite and radar ground-based measurements at the ARM TWP site on the island of Nauru. The MISR orbit passes over Nauru once in 9 days at ~2254 UTC. Since the MISR has a 360-km-wide swath, a satellite image corresponds to a large area surrounding the island. In contrast,

the temporal measurements from zenith-pointing surface radar represent line measurements (vertical cross section) along the wind direction.

[18] In order to find comparable satellite and radar measurements the following two requirements were met. First, the satellite overpasses and ground-based measurements occurred at the same time during the day. Second, during the observations the well-defined single layer of low cumulus clouds (without cirrus cloud contamination) occurred over both Nauru and in the area surrounding the island. Six available MISR overpasses of Nauru from March 2000 to December 2000 were examined along with coincident ground-based measurements. We found that data from 9 August 2000 meet the two requirements (Figure 3). We used these data for our further analyses. Radar-derived cloud products are considered as a reference.

[19] The quantitative comparison between the satellite-retrieved cloud geometrical thickness and that determined from radar measurements will be meaningful if the cloud products are derived for the same cloud fields. Since the

a) scene 110x110 km

175 -- 300	
150 -- 175	
125 -- 150	
100 -- 125	
75.0 -- 100	
50.0 -- 75.0	

Nauru

b) subscene 30x30 km

255 -- 300	
211 -- 255	
166 -- 211	
121 -- 166	
76.7 -- 121	
32.0 -- 76.7	
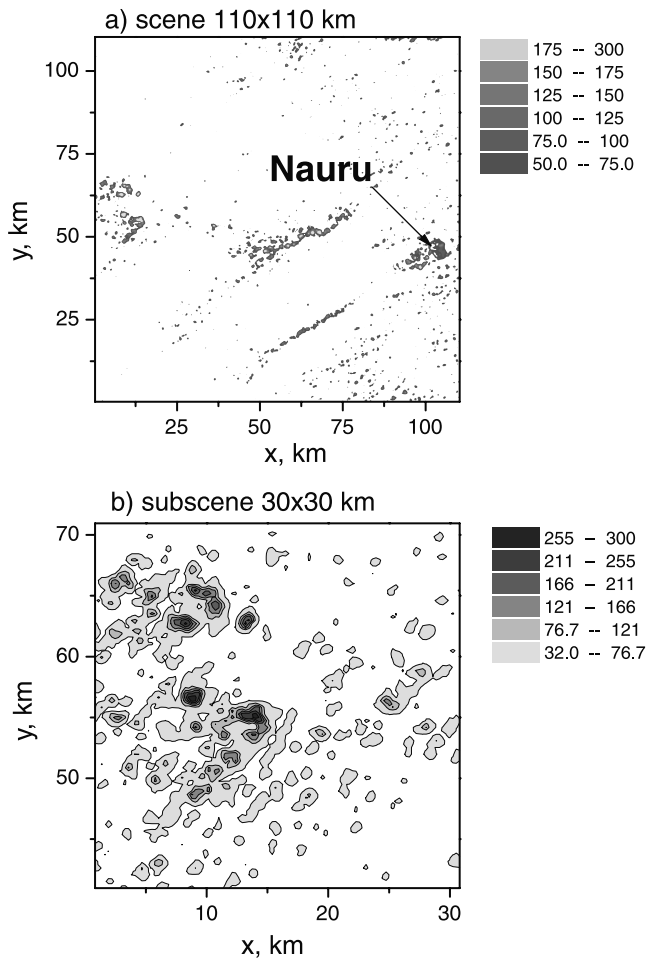
Figure 3. Cumulus clouds from Multiangle Imaging Spectroradiometer (MISR) observations in (a) 110×110 km and (b) 30×30 km regions surrounding and near Atmospheric Radiation Measurement program (ARM) Tropical Western Pacific (TWP) site (Nauru), 9 August 2000 at nadir radiance (An camera).

cloud field is not horizontally isotropic and is not homogeneous for a large 110×110 km scale (Figure 3a), we performed the satellite cloud retrieval for different parts of this field. First, we chose from a large 110×110 km MISR image (Figure 3a) a subscene (Figure 3b), which has bulk spatial horizontal statistics (section 3.3) similar to the temporal values (section 3.2). The main bulk horizontal statistics, which describe single-layer broken clouds, are the cloud fraction N and characteristic horizontal cloud size D. Here we use the mean (average) value of cloud chord length as the characteristic horizontal cloud size. The cloud chord length is defined as the distance between the trailing and leading edges of a cloud for a given direction (e.g., in the x direction). We assume that single-layer, low, broken cloud fields with similar N and D should have similar average vertical size H. Note that D and H are positively correlated [see, e.g., *Benner and Curry*, 1998]. Second, we choose from a large, 110×110 km, MISR image (Figure 3a) two additional subscenes (section 3.6), which have bulk spatial horizontal statistics different from the temporal ones. Third,

we retrieve the vertical cloud thickness for these three subscenes and compare the satellite-derived values with radar-derived ones (reference).

3.2. Temporal Cloud Statistics

[20] Estimated cloud statistics are functions of a sample size. The sample size should be chosen from the balance of the following two opposing requirements: On one hand, the sample size should be small to avoid the problem of the cloud field temporal nonstationarity (spatial nonhomogeneity), but, on the other hand, the sample size should be large enough to represent accurately the cloud field variability. Since the variability of a cloud field depends strongly on cloud type, the sample size is a function of the cloud type as well. For example, for overcast stratocumulus clouds, good agreements between temporal and spatial statistics were obtained for the temporal resolution of 0.5 hour [*Dong et al.*, 1998], but for broken stratocumulus clouds temporal and spatial statistics are in agreement for larger temporal resolution ($\sim$1 hour) [*Minnis et al.*, 1992]. The broken cloud field over Nauru and surrounding area is highly variable (Figure 3); therefore we used a large temporal sample ($\sim$1.5 hours). The radar data collected during this period (Figure 4) were applied to derive cloud statistics (Figure 5). We set the radar sensitivity threshold equal to -50 dBZ, which is sufficient to detect most clouds [see, e.g., *Clothiaux et al.*, 1999]. The latter corresponds to a liquid water content of $\sim$0.01 g/m^3 [*Fox and Illingworth*, 1997].

[21] For a given sample size and threshold value (-50 dBZ) we obtain the following temporal cloud statistics (subscript t): The cloud fraction N_t equals 0.24; the average vertical geometrical size H_t equals 0.17 km; and the average cloud horizontal size (chord) L_t equals 177 s. The height of the cloud base z_t varies over a large range with the average value $Z_t = 0.85$ km and the minimum value $z_{t, min} = 0.74$ km (Figure 5). The latter is considered to be the lifting condensation level (LCL). Because of a lack of any 3-D information from the ground sensors we have neglected cloud evolution and linked temporal and spatial size and statistics through the cloud-level wind speed. The latter is obtained from radiosonde measurements performed at 2331 UTC with high vertical resolution (0.03 km). Since the wind speed is variable (from 7.3 m/s to 10.1 m/s) in the cloud layer (from 0.74 km to 1.28 km), we use an average cloud-level wind speed V_w. Assuming that this average value ($V_w \sim 8.5$ m/s) is representative of the 1.5-hour temporal sample S_t, we estimate the corresponding spatial sample size S_s as $S_s = S_t V_w \sim 45$ km. In a similar way the mean spatial horizontal cloud size (chord), L_s, is estimated as $L_s = L_t V_w \sim 1$ km.

3.3. Spatial Cloud Statistics

[22] The selected subscene (Figure 3b) is not over the island. Because of the island effect the cloud field goes through transformations (you can see the long cloud streak in Figure 3a). As a result, the radar statistics do not match the satellite spatial statistics in this region. Since satellite-derived statistics are functions of the radiative threshold [see, e.g., *Wielicki and Welch*, 1986], the latter should be specified. We illustrate the threshold specification for one MISR subimage ($\sim$30 $\times$ 30 km^2). Figures 3b and 6 show radiances that correspond to this subscene. As can be seen in Figure 6, for the Aa camera (θ_6 direction), there is a low

Horizontal sample, km
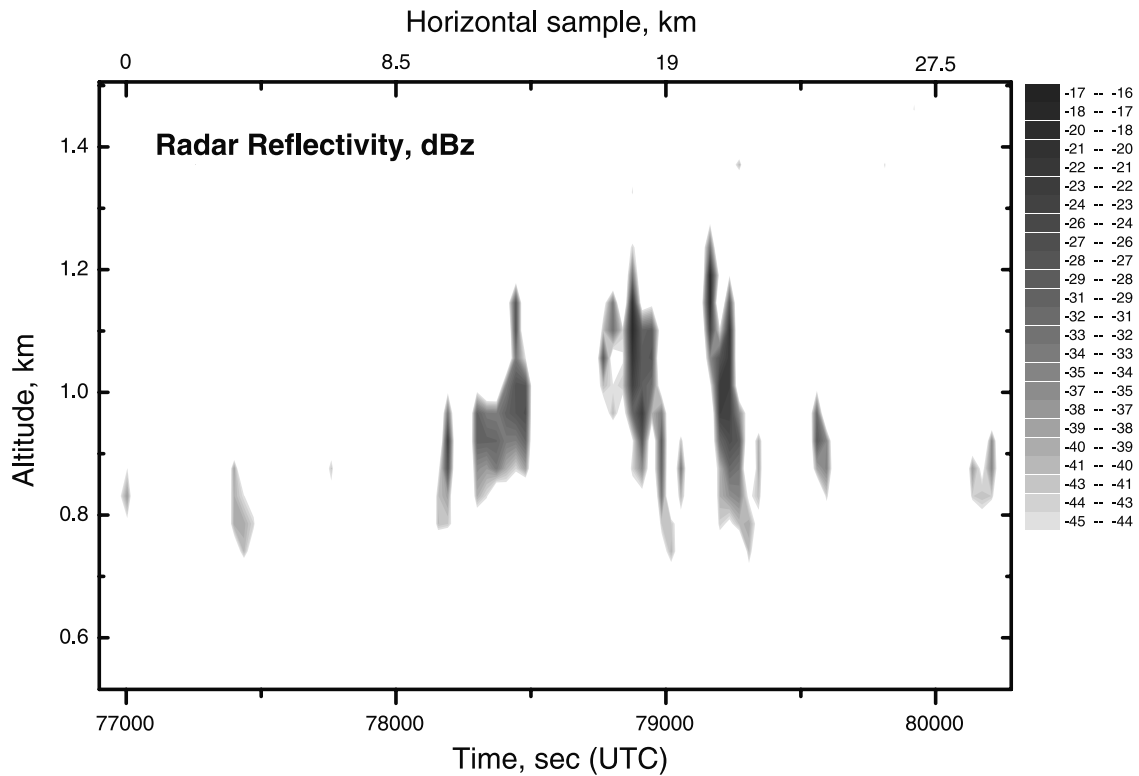
Figure 4. Cumulus clouds from ground-based radar measurements at ARM TWP site (Nauru) 9 August 2000: time-height cross section of radar reflectivity. A scale converting time interval (seconds) to equivalent horizontal sample (kilometers) is given at the top of Figure 4. Note difference in vertical and horizontal scales: The horizontal scale (top) is significantly larger than the height scale (vertical axes).

contrast between clouds and ocean. The opposite is true for other cameras with different viewing angles. This can be explained as follows: For the ocean, sun glint (a strong forward scattering signal) usually occurs at the same viewing angle as the solar zenith angle $\theta_\oplus$ [see, e.g., *Soulen et al.*, 2000]. In other words, for sun glint the scattering angle (the angle between the direction of incoming solar radiation and viewing direction) is close to 180°. For the observational conditions considered here (geographic latitude, local time, etc.), the solar zenith angle $\theta_\oplus \sim 30°$ and the scattering angle observed by the Aa camera is close to 180° (the forward scattering direction). For this reason, there is a strong reflection of the ocean in θ_6 direction, and the ocean surface is relatively bright. Since for the Aa camera the
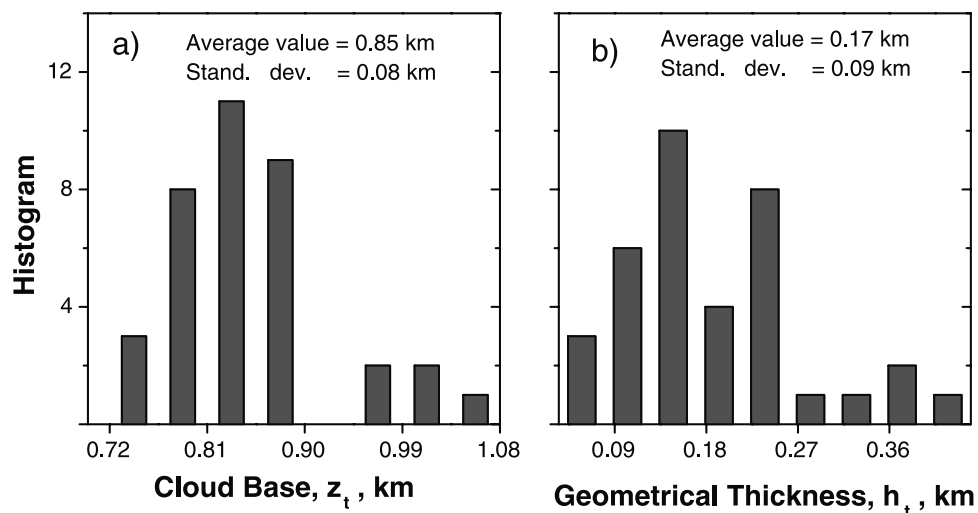

Figure 5. Cumulus clouds from ground-based radar measurements at ARM TWP site (Nauru) 9 August 2000: histograms of (a) height of cloud base z_t and (b) cloud vertical geometrical size (thickness) h_t. Corresponding values of the mean and standard deviations (Stand. dev.) are shown.

Forward cameras   *Aft cameras*
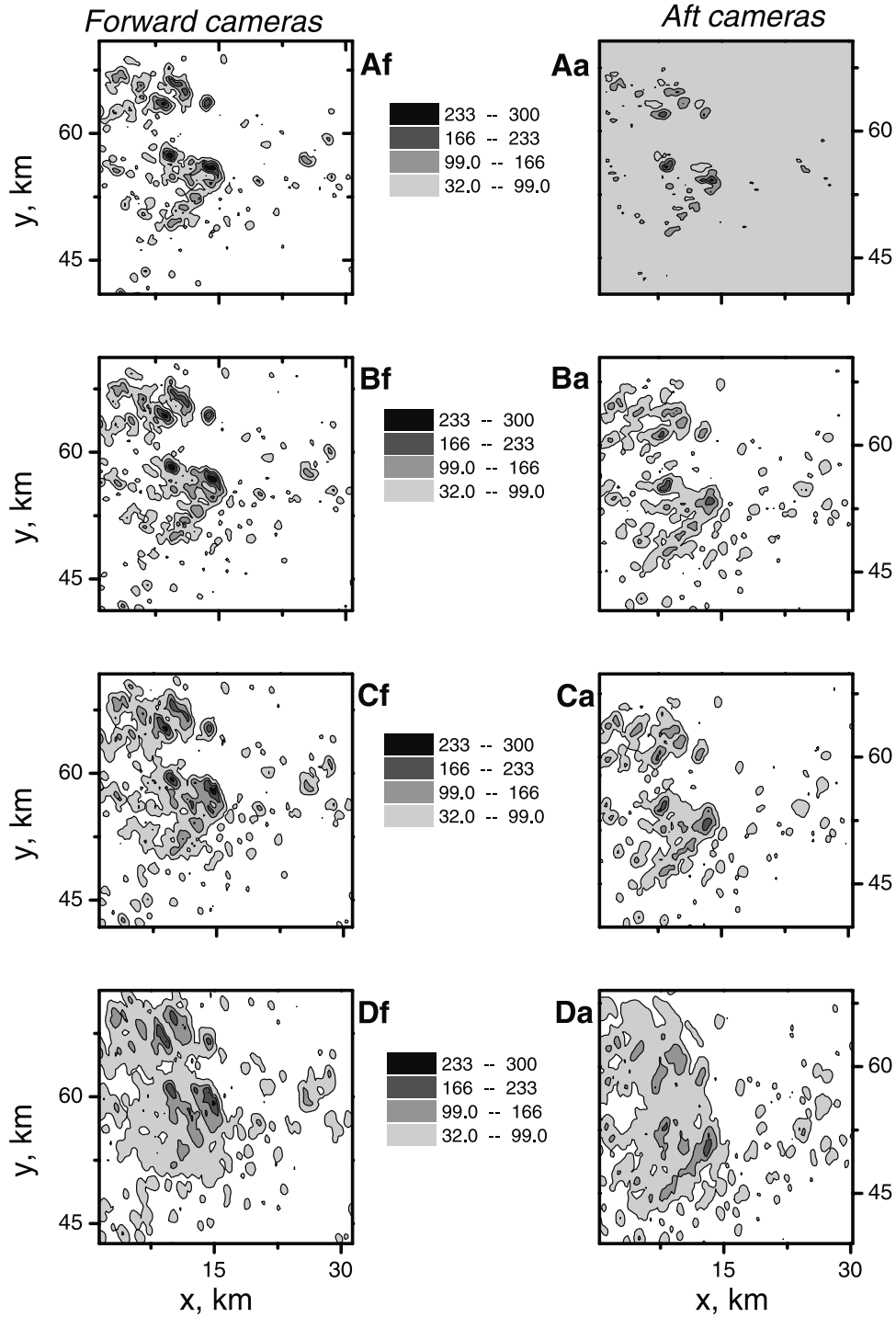
Figure 6. MISR images of cumulus clouds near ARM TWP site (Nauru) 9 August 2000. These images represent eight cameras with look angles spread out along the MISR flight path in the (left) forward and (right) aft directions.

contrast between clouds and ocean is very low, we do not include the measured radiances $I(\theta_6)$ in our further analysis. The other eight MISR images were processed to obtain the corresponding radiance probability densities pdf$\{I_{\mathrm{misr}}(\theta)\}$ as functions of the dimensionless digital count m (see equation (3)). Then, these quantities were used to obtain the directional cloud fractions $N_{\mathrm{misr}}(\theta)$ and average $N_{\mathrm{avr,misr}}$ cloud fraction. Finally, we get the difference $\Delta N_{\mathrm{misr}} = N_{\mathrm{avr,misr}} - N_{\mathrm{nadir,misr}}$. In contrast to $N_{\mathrm{nadir,misr}} = N(\theta_5)$ the difference ΔN_{misr} is not

a monotonically decreasing function of m and has a maximum $\Delta N_{\mathrm{misr}} = 0.065$ at $m = 21$ (Figure 7). Correspondingly, the absolute nadir radiance $I(\theta_5)$ at $m = 21$ is 31.3 (W m^{-2} sr^{-1} µm^{-1}). This value $I(\theta_5) = 31.3$ was used here as a threshold, $I_0(\theta_5)$. The selection of the threshold value $I_0(\theta_5)$ and, thereby, designation of the horizontal distribution of cloud pixels conclude the first step of the h retrieval. For the given threshold $I_0(\theta_5)$ the scene spatial statistics are as follows: for the cloud fraction $N_{\mathrm{misr}} = 0.25$ and the mean
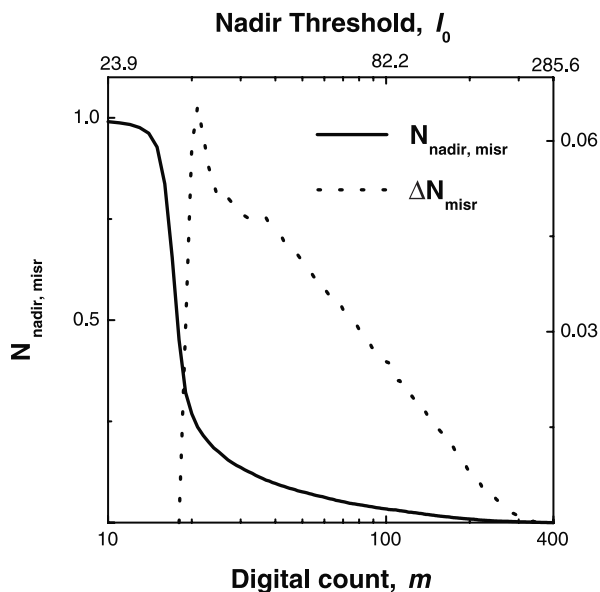
Figure 7. The nadir-view $N_{nadir,misr}$ cloud fraction and the difference $\Delta N_{misr} = N_{avr,misr} - N_{nadir,misr}$ as function of digital count m. A scale converting m to equivalent nadir threshold $I_0(\theta_5)$ is given at the top of Figure 7.

cloud horizontal chords $L_{x,misr} = 1.21$ km (x direction) and $L_{y,misr} = 1.16$ km (y direction). These spatial statistics $L_{x,misr}$ and $L_{y,misr}$ are close to the temporal statistics (section 3.2).

3.4. Model Specification

[23] The final step of our suggested approach is to determine the model parameters h_{mod} for which $\Delta N_{mod} = \Delta N_{misr}(m^*)$. The "tuning" of h_{mod} was done using a fixed horizontal distribution of cloud pixels. For the cloud models considered here, the tuning was done using the following procedure for two cloud models (section 2.3). The initial vertical distributions $h_{mod,1}^{(0)}$ and $h_{mod,2}^{(0)}$ for which the average value $H_{mod,1}^{(0)} = H_{mod,2}^{(0)} = 0.22$ km, were specified. The initial value $H^{(0)}$ was obtained randomly, as $H^{(0)} = H_t + \alpha H_t$, where H_t is the average cloud thickness from radar observations (section 3.2) and α is a random variable uniformly distributed on (0,1) interval. Examples of the probability distributions pdf $\{h_{mod,1}^{(0)}\}$ and pdf $\{h_{mod,1}^{(0)}\}$ corresponding to these two models are presented in Figure 8. For the given cloud field, $N_{mod,1}^{(0)}(\theta_i)$ and $i = 1, \ldots, 8$ were calculated using the Monte Carlo method. On the basis of these values the value $\Delta N_{mod,1}^{(0)} = 0.072$ was determined. This procedure was repeated for two additional vertical distributions $h_{mod,1}$ connected with the initial one, namely, for $h_{mod,1}^{(1)} = 0.5$ $h_{mod,1}^{(0)}$ and $h_{mod,1}^{(2)} = 1.5$ $h_{mod,1}^{(0)}$. On the basis of these vertical distributions the average vertical cloud sizes $H_{mod,1}^{(k)}$ and the differences $\Delta N_{mod,1}^{(k)}$ $k = 1, 2$, were similarly obtained. Thereupon $\Delta N_{mod,1}^{(k)}$ versus $H_{mod,1}^{(k)}$, k = 0, \ldots, 2, was plotted (Figure 9). The same steps were repeated for model 2. We note that, in the given models, $\Delta N_{mod,1}$ and $\Delta N_{mod,2}$ are fairly smooth and monotonically increasing functions of the average vertical cloud size H. The model curves were then used to retrieve H_{misr} (Figure 9). The equality $\Delta N_{mod} = \Delta N_{misr}$ takes place for $H_{mod,1} \sim 0.20$ km and $H_{mod,2} \sim 0.18$ km for models 1 and 2, respectively. The retrieved values H are within physically acceptable limits. Despite the substan-
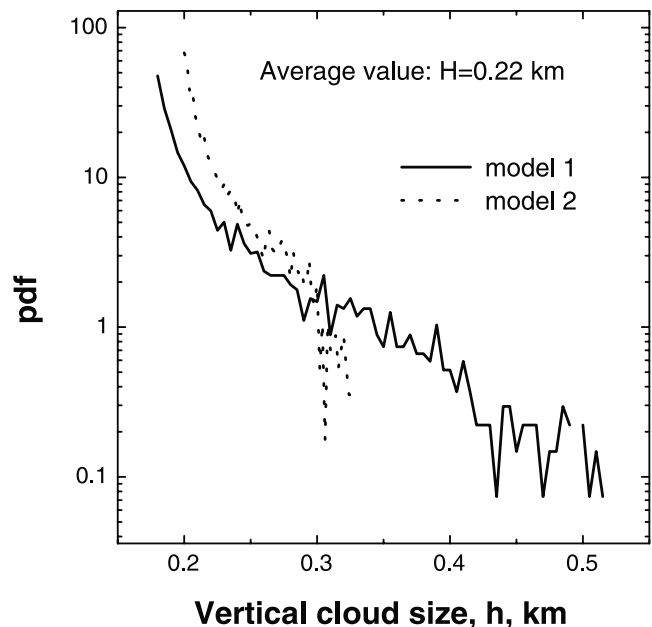
Figure 8. Probability density functions of the cloud geometrical thickness h_{mod}, corresponding to the different models. Both model distributions $h_{mod,1}$ and $h_{mod,2}$ have the same average value $H_{mod} = 0.22$ km. The model geometrical thicknesses $h_{mod,1}$ and $h_{mod,2}$ are obtained from equations (6a) and (6b) at particular values $a_1 = 0.01$ and $b_1 = 0.03$ and $a_2 = 0.001$ and $b_2 = 0.058$, respectively.

tial difference between these two models (Figure 8) the values $H_{mod,1}$ and $H_{mod,2}$ differ insignificantly, by $\sim10\%$. Hence we can make a preliminary conclusion that, for the given horizontal distribution of clouds, the average retrieved geometrical thickness H depends weakly on the chosen cloud model.
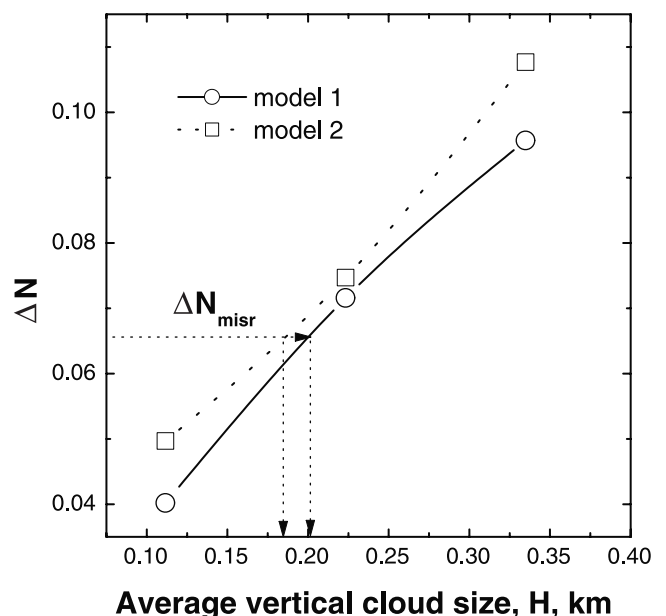
Figure 9. Difference ΔN_{mod} as a function of the average geometrical thickness H_{mod} for two different cloud models. The values of $H_{mod,1} = 0.20$ km and $H_{mod,2} = 0.18$ such that $\Delta N_{mod,1}$ and $\Delta N_{mod,2}$ are equal to ΔN_{misr} are shown.
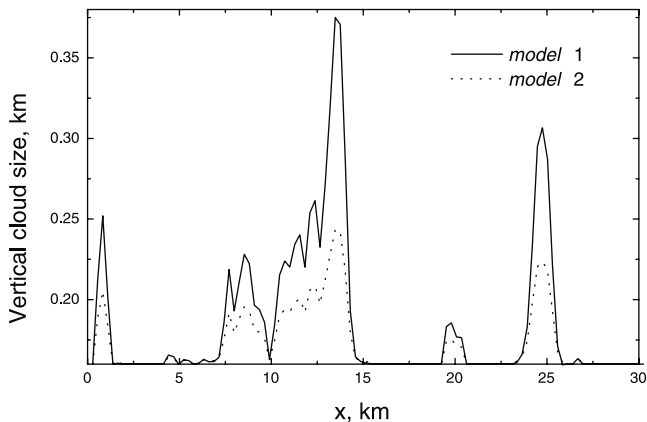
a) model 1

b) model 2
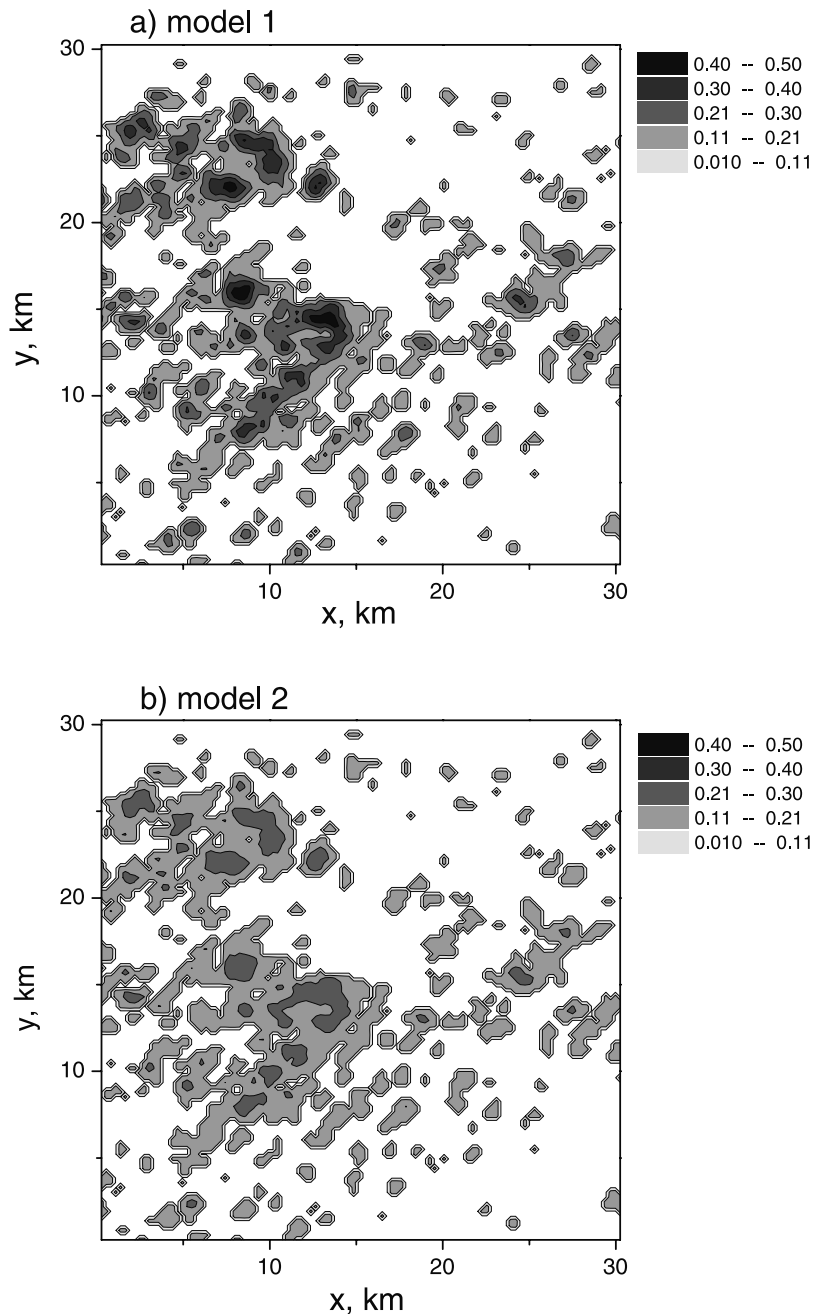
Figure 10. Horizontal distribution of cloud pixels for digital count $m^* = 21$ (nadir threshold $I_0(\theta_5) = 31.3$) and two different cloud models ($H_{\mathrm{mod},1} = 0.20$ km and $H_{\mathrm{mod},2} = 0.18$ km). For a given value of $m = m^*$ the nadir cloud fraction $N_{\mathrm{nadir,misr}}$ is equal to 0.25.

[24] However, the individual cloud geometry is sensitive to the cloud model specification (Figures 10 and 11). Since model 2 has a narrower distribution pdf$\{h_{\mathrm{mod},2}\}$, the amplitude of fluctuations of the geometrical thickness $h_{\mathrm{mod},2}$ is much less than that of $h_{\mathrm{mod},1}$ (Figure 11). Also, for Model 2 the distribution of $h_{\mathrm{mod},2}$ within clouds is more uniform, and clouds have a less convex appearance. Consequently, the use of a different cloud model will introduce differences between (1) the mean vertical extent of clouds (the amplitude of h_{mod} fluctuations) and (2) individual cloud shapes (more or less convex appearance). For model 1 the range of derived $h_{\mathrm{mod},1}$ (Figure 12) is similar to the range of h_t

(Figure 5b) obtained from radar observations. The same is true for the standard deviation (Figures 5b and 12). Therefore we will use model 1 for further analysis.
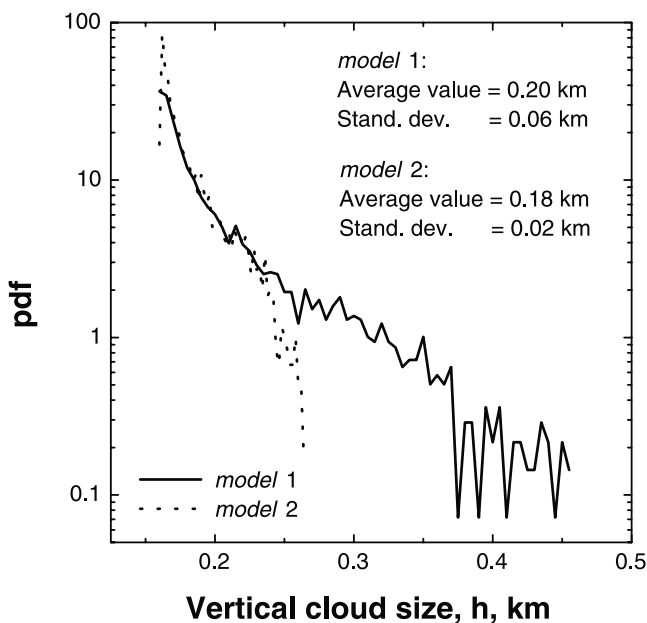
3.5. Cloud Base Variability

[25] For a given horizontal distribution of cloud pixels the directional cloud fraction $N(\theta)$ is a function of both (1) vertical size of cloud pixels h and (2) their base height z_{base}. The effect of h variations on the directional cloud fraction $N(\theta)$ was illustrated in section 2.1. In particular, it was shown that $N(\theta)$ corresponding to a cloud field with variable h can either be greater than or less than $N(\theta)$ corresponding
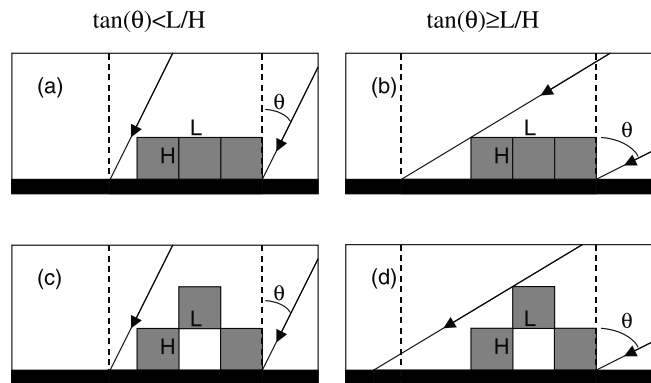
Figure 11. Vertical cross section ($y = 15.13$ km) of two cloud fields shown in Figure 10.
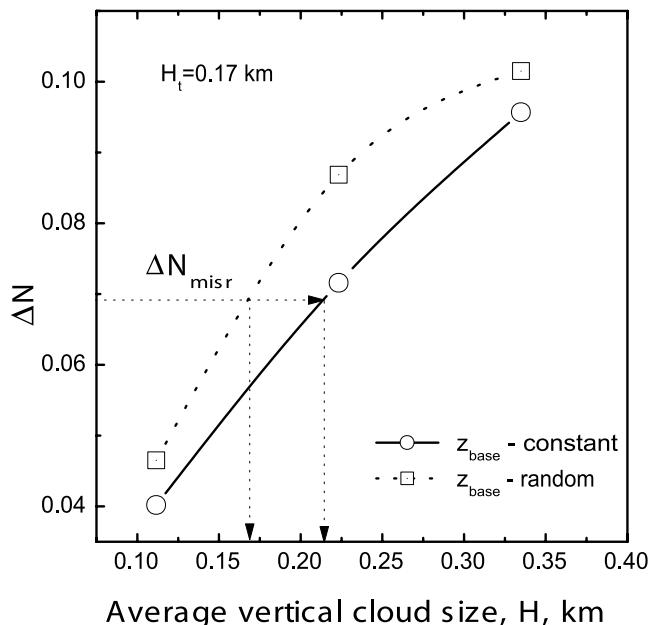

Figure 13. A schematic diagram illustrating that the directional cloud fraction depends on the cloud base height distribution in addition to the average vertical cloud size H. For variable cloud base the directional cloud fraction (Figure 13d) $N(\theta)$ (cloud projection onto x axis) can be larger than (Figure 13b) $N(\theta)$ for constant cloud base.
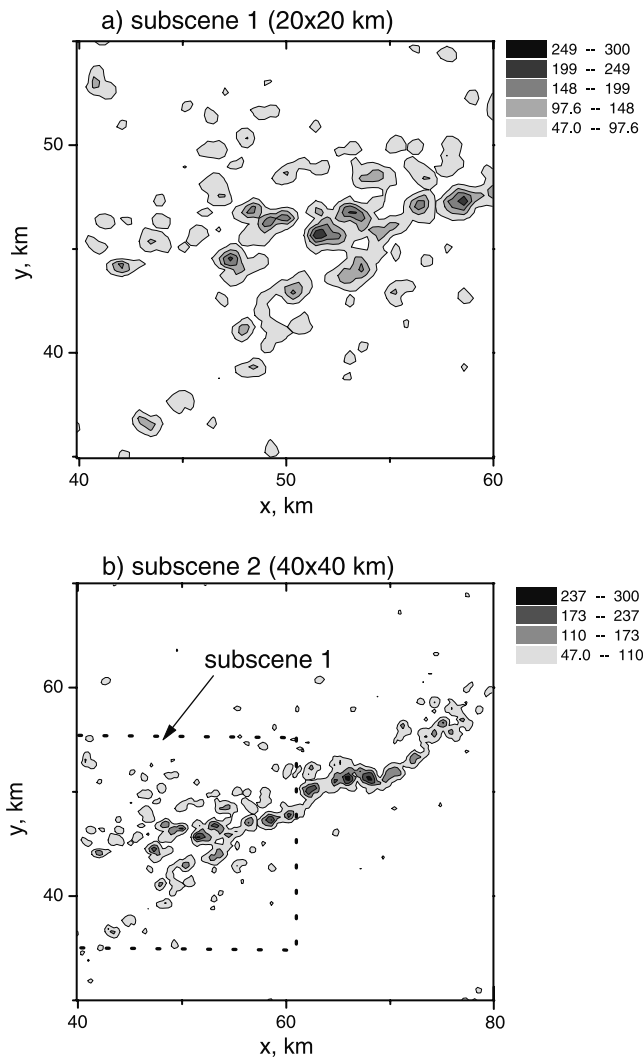
to a cloud field with constant h (plane-parallel geometry). Figure 13 illustrates qualitatively the sensitivity of $N(\theta)$ to the cloud base variability.

[26] The height of cloud base can vary significantly (Figures 4 and 5); then the question arises as to whether it is better to include δz_{base} variability in H retrieval or to assume a fixed value of δz_{base}. With this aim in mind, two cloud retrievals are performed. The only difference between these experiments is the assumption about the height of the pixel base above LCL $\delta z_{base,mod}$. In the first experiment, $\delta z_{base,mod}$ is fixed and equals 0. In other words, all cloud pixels have the same cloud base at the LCL. In the second experiment, $\delta z_{base,mod}$ is a random variable. For each cloud pixel the height of its base above LCL is chosen independently and is equal to $\alpha \, \delta Z_t$ where α is a random variable uniformly distributed on $(0,1)$ interval, $\delta Z_t = Z_t - z_{t,min}$, and Z_t and $z_{t,\,min}$ are the radar-retrieved parameters (section 3.2).

Note that these two retrievals do not take into account the correlation between $\delta z_{base,mod}$ and h_{mod}. Figure 14 gives results of these two retrievals. The model curves $\Delta N_{mod,const}$ ($\delta z_{base,mod}$ is constant) and $\Delta N_{mod,random}$ ($\delta z_{base,mod}$ is random) are monotonically increasing functions of the average vertical cloud size H_{mod}. As can be seen for this case, (1) the H retrieval is sensitive to the cloud base fluctuations, and (2) including the cloud base variability in the inversion process increases the accuracy of retrieval.

3.6. Sample Size

[27] We compared a satellite-retrieved mean vertical cloud size (geometrical thickness) to a ground truth size

Figure 12. Probability density functions of the derived geometrical thickness h, corresponding to two cloud fields shown in Figure 10. Corresponding values of the mean and standard deviation (Stand. dev.) are shown.

Figure 14. Difference ΔN_{mod} as a function of the average geometrical thickness H_{mod} for two MISR data experiments. The values of model parameters $H_{mod,const}$ and $H_{mod,random}$ such that $\Delta N_{mod,const}$ and $\Delta N_{mod,random}$ are equal to ΔN_{misr} are shown.

a) subscene 1 (20x20 km)

■	249 -- 300
▨	199 -- 249
▩	148 -- 199
▨	97.6 -- 148
░	47.0 -- 97.6

b) subscene 2 (40x40 km)

■	237 -- 300
▩	173 -- 237
▨	110 -- 173
░	47.0 -- 110

Figure 15. Cumulus clouds from MISR observations in (a) 20 × 20 km and (b) 40 × 40 km subscenes near ARM TWP site (Nauru) 9 August 2000: nadir radiance (An camera). Subscene 1 (dotted lines) is shown (Figure 15b) as part of subscene 2.

for a single MISR subscene (30 × 30 km). For this subscene (Figure 3b) the horizontal spatial statistics (cloud fraction and the mean horizontal size) are close to the temporal values obtained from radar sampling. We found that mean vertical cloud size can be obtained with reasonable accuracy (∼0.03 km) in this case. Note that the cloud field, which corresponds to this MISR image, is ∼70 km away from Nauru Island. The question arises: How well does the suggested technique perform for other MISR subscenes?

[28] To evaluate the performance of the suggested approach, we used two additional MISR subscenes with different sample sizes and sample cloud fractions (Figure 15). The mean values of the cloud chord (mean horizontal cloud sizes) are about the same for these two subscenes, ∼1 km in both x and y directions. However, the corresponding values of cloud fraction differ considerably: For the first (20 × 20 km) and second (40 × 40 km) subscenes the cloud fraction is 0.16 and 0.07, respectively. Figure 16 shows results of the

cloud retrieval. One can readily see that satellite-retrieved averaged vertical cloud size depends weakly on both the sample size and the sample cloud fraction (Figure 16). The same is true for satellite-retrieved probability distribution functions of the vertical cloud size (Figure 17). Probably, these weak dependences are attributed to the statistical homogeneity (in terms of cloud vertical thickness) of the given MISR scene (110 × 110 km). Further, the model curve is almost flat for the second subscene with a small cloud fraction (Figure 16). It can be explained as follows. In general, the effects of mutual cloud shadowing are negligible for cloud fields with a small cloud fraction. Therefore, for these fields the directional cloud fraction (for oblique angles) increases slightly (relative to the cloud fields with moderate/large cloud fractions) as H grows. As a result, the proposed retrieval technique will work poorly for a scene with small (<0.07) cloud fractions. To make the cloud retrieval more reliable, one can break down a scene with small cloud fractions (<0.1) into a number of smaller subscenes. Some of them (clear-sky subscenes) will not contain any clouds. The rest of them (cloudy subscenes) will have larger cloud fraction (≥0.1). The suggested technique could then be applied to these cloud subscenes.

4. Model Data Cloud Retrieval

[29] In addition to the MISR data cloud retrieval we performed model-output inverse experiments to estimate the accuracy of the suggested technique. First, a 3-D broken field of marine clouds was simulated using a large-eddy simulation (LES) model [*Khairoutdinov and Kogan*, 1999]. The obtained 3-D cloud field is considered to be a ''real'' 3-D cloud field. Second, we simulated the MISR measurements by applying the Monte Carlo method. In the model inverse (retrieval) experiments the simulated reflectance data are regarded as observations. Third, we used these reflectances to retrieve average vertical cloud size H_{ar} by applying the proposed technique. Finally, we compared the retrieved cloud product with the true value produced by the LES model. Since all properties of the simulated broken cloud field (available from LES simulation) are known exactly, the simulated measurements allow one to have precise control over the retrieval experiments.

[30] Sounding data from the ARM TWP site are used to initialize and run the LES model. In particular, the latter is initialized using temperature and moisture profiles from the 2331 UTC 9 August 2000 sounding at the Nauru TWP site. Surface sensible and latent heat fluxes are computed applying an assumption of constant surface (ocean) temperature. Compared with simulation of stratocumulus clouds [*Ovtchinnikov and Kogan*, 2000], the computational domain has been expanded in this study from 3 × 3 × 2 km^3 to 10 × 10 × 2 km^3 with 0.1-km horizontal and 0.033-km vertical resolution. This larger domain improves the statistical representation of the horizontal inhomogeneity of the cumulus cloud field. In order to reduce the computational cost a so-called ''bulk'' microphysical parameterization is used here, meaning that the liquid water content is predicted by the model, while droplet number concentration and the shape of the cloud droplet spectrum are prescribed a priori. The gamma size distribution function [see, e.g., *Deirmendjian*, 1969; *Welch et al.*, 1980] was applied to describe the cloud
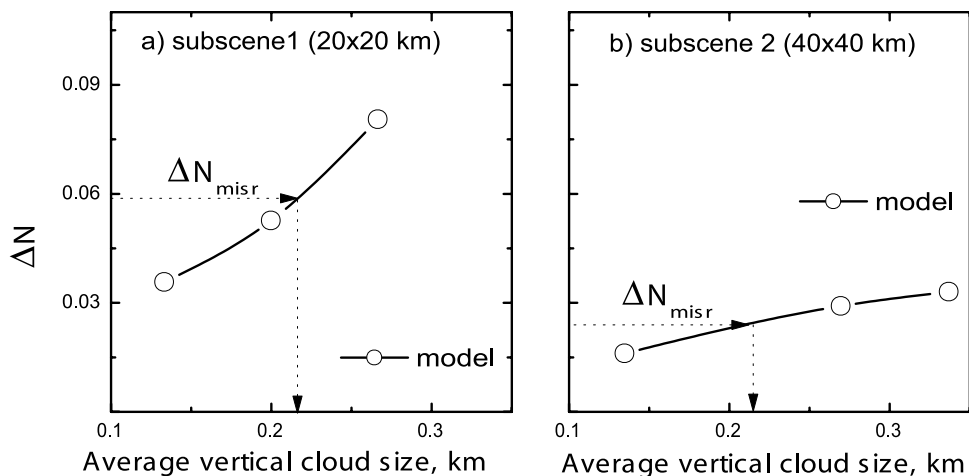
Figure 16. Difference ΔN_{mod} as a function of the average geometrical thickness H_{mod} for (a) subscene 1 (20 × 20 km) and (b) subscene 2 (40 × 40 km).

droplet spectrum. The parameters of the distribution function were chosen to represent cumulus clouds of moderate thickness (so-called C.1 model). Note that the C.1 scattering function (the asymmetry factor ∼0.86) was used in the I3RC project. Optical properties of simulated broken clouds are highly variable in both horizontal and vertical dimensions (Figure 18). The LCL equals 0.72 km. The height of the cloud base above LCL $\delta z_{base,les}$ and cloud geometrical thickness h_{les} vary over a large range (Figure 19). Their average values δZ_{les} and ΔH_{les} are equal to 0.22 km and 0.20 km, respectively.

[31] For this 3-D cloud field from the LES model we simulate MISR measurements at 672 nm by using the Monte Carlo method and periodical boundary conditions. The Monte Carlo algorithms have been developed and tested
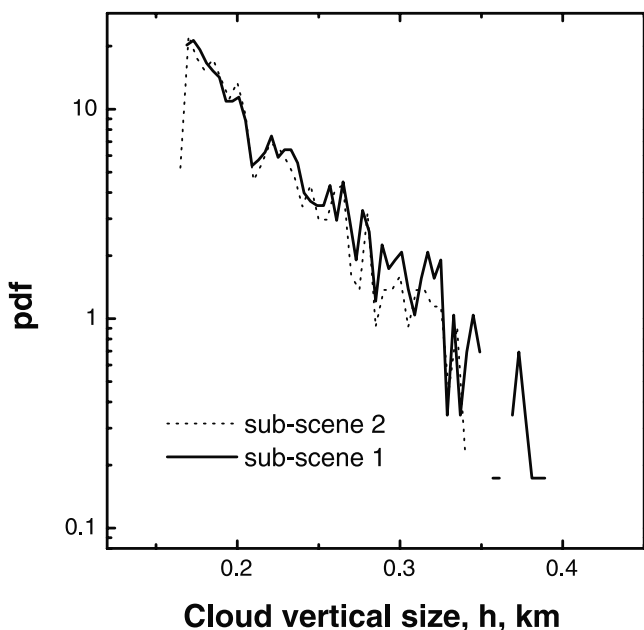
Figure 17. Probability density functions of the derived geometrical thickness h, corresponding to two subscenes shown in Figure 15.
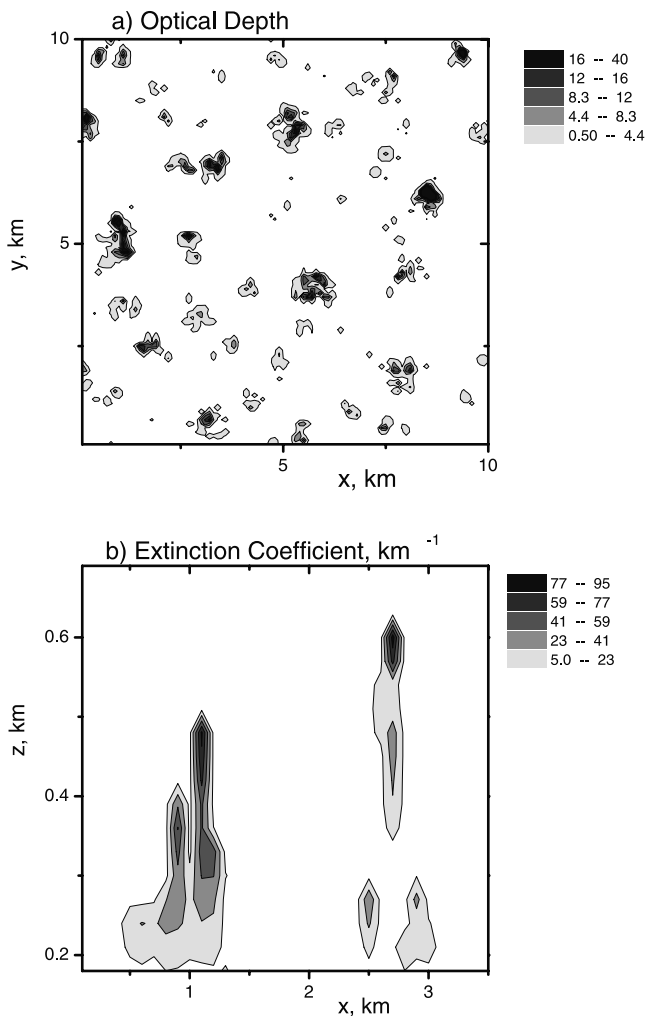
Figure 18. Cumulus clouds generated by large-eddy simulation (LES) model: (a) horizontal distribution of optical depth and (b) an example of vertical distribution of extinction coefficient (a vertical cross section of the field of optical depth) above lifting condensation level (LCL). To demonstrate clearly strong horizontal and vertical variability of the extinction coefficient, we use different scales in the horizontal and vertical directions (Figure 18b).
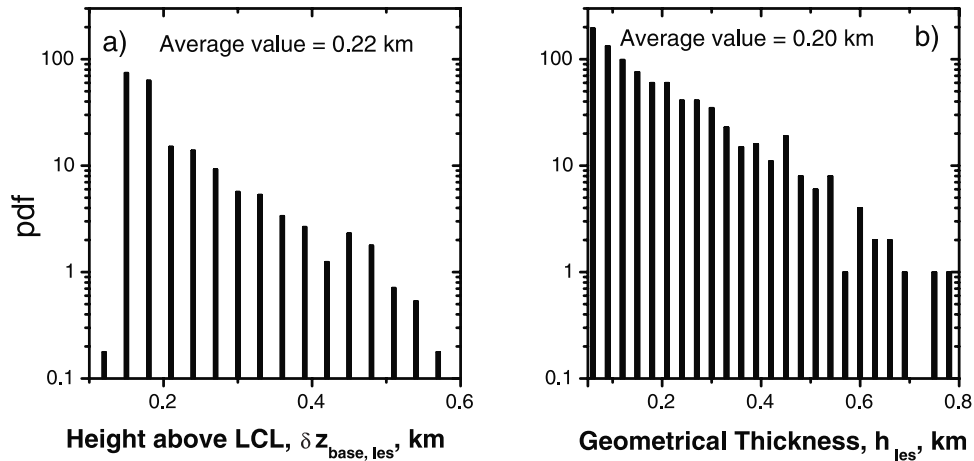
Figure 19. Cumulus clouds generated by LES model: Probability density functions of (a) height of cloud base above LCL $\delta z_{base,les}$ and (b) cloud vertical geometrical size (thickness) h_{les}.

during the I3RC project (see Web page at http://climate.gsfc. nasa.gov/I3RC). For each pixel in the considered domain (total number of pixels is 10,000), reflectances are calculated at nadir (Figure 20a) and eight off-nadir MISR viewing angles (Figure 20b). The radiative calculations are performed for solar zenith and azimuth angles equal to 30° and 330°, respectively. Solar azimuth angle is measured from OY axis. This relative Sun-sensor geometry is similar to the real one when the MISR passes over the island of Nauru at ∼2254 UTC. The total number of simulated photons is 10^9 (nearly 100,000 photons per pixel). A Lambertian model with an albedo of 0.06 is used for the ocean surface. The Lambertian assumption is not appropriate for the ocean surface if a viewing angle is close to the forward scattering direction (see, e.g., Figure 6). However, for other viewing directions the Lambertian model can be considered as reasonable approximation for the ocean surface [see, e.g., *Soulen et al.*, 2000]. Analogous to the real MISR data cloud retrieval (section 3), we used only eight MISR images in our model-output cloud retrieval (the Aa image was not included). The simulated reflectances are considered as observations.

[32] Similar to the MISR data retrieval experiments considered above (section 3.5), two model-output retrieval experiments are carried out. In the first experiment, $z_{base,les}$ is fixed and equals $z_{min} = 0.72$ km. In the second experiment, $z_{base,les}$ is a random variable. For each cloud pixel the height of its base above z_{min} is chosen independently and equal to $\alpha \, \delta Z_{les,avr}$, where α is a random variable uniformly distributed on the interval (0,1). Results of these two experiments (Figure 21) show that the retrieved parameter
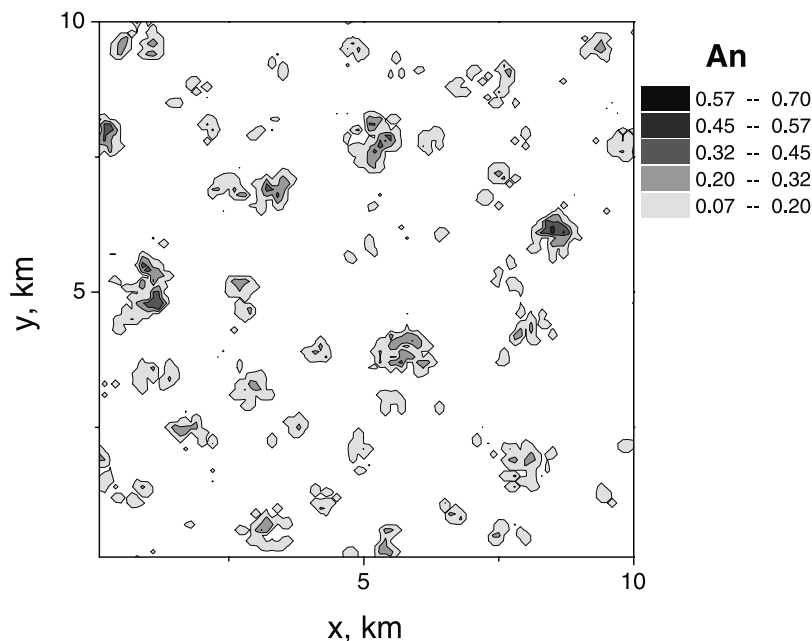
Figure 20a. Simulated MISR images of cumulus clouds near ARM TWP site (Nauru) for nadir viewing angle (An camera).
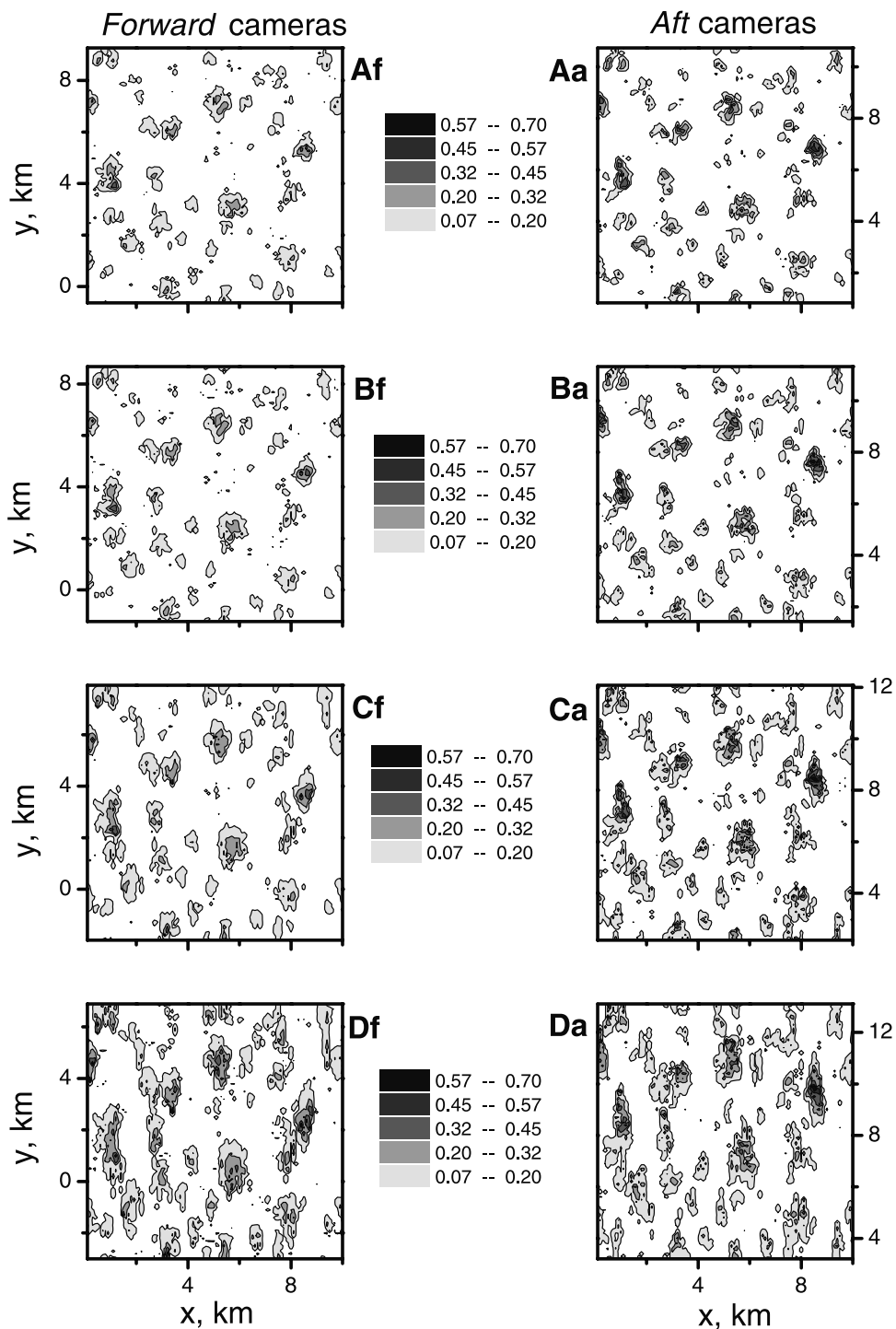
Figure 20b. Simulated MISR images of cumulus clouds near ARM TWP site (Nauru) for oblique viewing angles of (left) forward and (right) aft directions.

H coincides with the LES-based value H_{les} reasonably well; the maximum difference between the average values H and H_{les} is ~0.1 km. By including the cloud base variability in the H retrieval, the difference is decreased.

5. Conclusion

[33] The basic objective of cloud detection from space is to define the spatial arrangement of individual clouds, both vertically and horizontally. In this study, we introduce a new technique for retrieving cumulus geometry from the high-resolution Multiangle Imaging Spectroradiometer (MISR) observations and apply it to a MISR data set. We derive both the horizontal distribution of cloud pixels and their geometrical thickness from the angular variations of the measured radiances.

[34] To evaluate the performance of this new multiangle cumulus geometry retrieval technique, we compare the
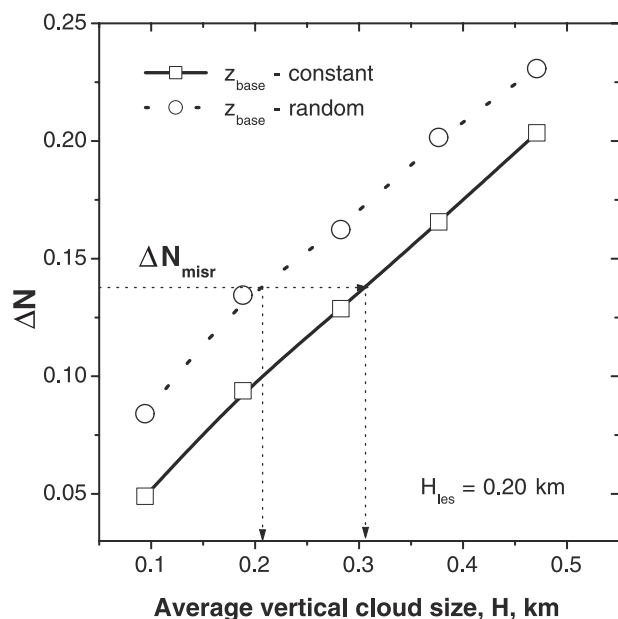
Figure 21. Similar to Figure 14 but for two model-output experiments.

MISR data with ground-based observations at the ARM TWP site (9 August 2000). The satellite-retrieved average vertical thickness of cumulus clouds matches closely (maximum difference $\sim$0.03 km) the corresponding ground truth value observed from radar measurements. We find that the accuracy of the cloud retrieval can be increased when additional information about cloud base variability is incorporated into the retrieval process. This information can be obtained from ground-based measurements (e.g., radar data) for particular events or as a climatological average. In addition, we verify this retrieval technique with simulated MISR observations by using a large-eddy simulation (LES) model and Monte Carlo method (model-output inverse problem). For this case the average cloud vertical size is obtained with reasonable accuracy ($\sim$0.1 km).

[35]   Our results demonstrate that multiangular MISR data have the potential for measuring individual cloud geometry. Because our comparison of satellite-retrieved with ground truth cloud properties considers only a single MISR overpass, further testing over additional MISR scenes is needed to understand better the limits and accuracy of this retrieval technique. The retrieved cloud geometrical properties can serve as a basis for estimating optical properties from additional radiative modeling. The retrievals of cloud optical properties from MISR data will be a subject of our future investigation.

References

Barker, H. W., and D. Liu, Inferring optical depth of broken clouds from Landsat data, *J. Clim.*, *8*, 2620–2630, 1995.

Benner, T. C., and J. A. Curry, Characteristics of small tropical cumulus clouds and their impact on the environment, *J. Geophys. Res.*, *103*, 28,753–28,767, 1998.

Chambers, L. H., B. A. Wielicki, and K. F. Evans, Accuracy of the independent pixel approximation for satellite estimates of oceanic boundary layer cloud optical depth, *J. Geophys. Res.*, *102*, 1779–1794, 1997.

Chambers, L. H., B. A. Wielicki, and N. G. Loeb, Shortwave flux from satellite-measured radiance: A theoretical study over marine boundary layer clouds, *J. Appl. Meteorol.*, *40*, 2144–2161, 2001.

Chevallier, F., P. Bauer, G. Kelly, C. Jakob, and T. McNally, Model clouds over oceans as seen from space: Comparison with HIRS/2 and MSU radiances, *J. Clim.*, *14*, 4216–4229, 2001.

Clothiaux, E. E., K. P. Moran, B. E. Martner, T. P. Ackerman, G. G. Mace, T. Uttal, J. H. Mather, K. B. Widener, M. A. Miller, and D. J. Rodriguez, The Atmospheric Radiation Measurement program cloud radars: Operational modes, *J. Atmos. Sci.*, *56*, 819–827, 1999.

Deirmendjian, D., *Electromagnetic Scattering on Spherical Polydispersions*, 290 pp., Elsevier Sci., New York, 1969.

Diner, D., G. Asner, R. Davies, Y. Knyazikhin, J.-P. Muller, A. Nolin, B. Pinty, C. Schaaf, and J. Stroeve, New directions in Earth observing: Scientific applications of multiangle remote sensing, *Bull. Am. Meteorol. Soc.*, *80*, 2209–2228, 1999.

Dong, X., T. P. Ackerman, and E. E. Clothiaux, Parameterizations of the microphysical and shortwave radiative properties of boundary layer stratus from ground-based measurements, *J. Geophys. Res.*, *103*, 31,681–31,693, 1998.

Fox, N. I., and A. J. Illingworth, The potential of a spaceborne cloud radar for the detection of stratocumulus clouds, *J. Appl. Meteorol.*, *36*, 676–687, 1997.

Han, D., and R. G. Ellingson, Cumulus cloud formulations for longwave radiation calculations, *J. Atmos. Sci.*, *56*, 837–850, 1999.

Khairoutdinov, M., and Y. Kogan, A large eddy simulation model with explicit microphysics: Validation against aircraft observations of a stratocumulus-topped boundary layer, *J. Atmos. Sci.*, *56*, 2115–2131, 1999.

Minnis, P., P. W. Heck, D. F. Young, C. W. Fairall, and J. B. Snider, Stratocumulus cloud properties derived from simultaneous satellite and island-based instrumentation during FIRE, *J. Appl. Meteorol.*, *31*, 317–339, 1992.

Ovtchinnikov, M., and Y. L. Kogan, Evaluation of radar retrieval algorithms in stratiform clouds using large-eddy simulations, *J. Geophys. Res.*, *105*, 17,351–17,359, 2000.

Pawlowska, H., et al., Microphysical and radiative properties of stratocumulus clouds: The EUCREX mission 206 case study, *J. Atmos. Res.*, *55*, 85–102, 2000.

Rossow, W., Measuring cloud properties from space: A review, *J. Clim.*, *2*, 201–213, 1989.

Rossow, W., and R. Schiffer, Advances in understanding clouds from ISCCP, *Bull. Am. Meteorol. Soc.*, *80*, 2261–2287, 1999.

Soulen, P. F., M. D. King, S.-C. Tsay, G. T. Arnold, and J. Y. Li, Airborne spectral measurements of surface-atmosphere anisotropy during the SCAR-A, Kuwait oil fire, and TARFOX experiments, *J. Geophys. Res.*, *105*, 10,203–10,218, 2000.

Titov, G., Statistical description of radiation transfer in clouds, *J. Atmos. Sci.*, *47*, 24–38, 1990.

Varnai, T., and A. Marshak, Statistical analysis of the uncertainties in cloud optical depth retrievals caused by three-dimensional radiative effects, *J. Atmos. Sci.*, *58*, 1540–1548, 2001.

Wang, Z., and K. Sassen, Cloud type and macrophysical property retrieval using multiple remote sensors, *J. Appl. Meteorol.*, *40*, 1665–1682, 2001.

Welch, R. M., S. K. Cox, and J. M. Davis, *Solar Radiation and Clouds*, *Meteorol. Monogr.*, vol. 17, no. 39, 96 pp., Am. Meteorol. Soc., Boston, Mass., 1980.

Wielicki, B., and R. Welch, Cumulus cloud properties derived using Landsat satellite data, *J. Appl. Meteorol.*, *25*, 261–276, 1986.

———————————

T. Ackerman, E. Kassianov, R. Marchand, and M. Ovtchinnikov, Pacific Northwest National Laboratory, 902 Battelle Boulevard, Richland, WA 99352, USA. (thomas.ackerman@pnl.gov; Evgueni.Kassianov@pnl.gov; roj@pnl.gov; mikhail@pnl.gov)